

Transition to branching flows in optimal planar convection

Silas Alben*

Department of Mathematics, University of Michigan, Ann Arbor, Michigan 48109, USA

(Received 28 March 2023; accepted 29 June 2023; published 26 July 2023)

We study steady flows that are optimal for heat transfer in a two-dimensional periodic domain. The flows maximize heat transfer under the constraints of incompressibility and a given energy budget (i.e., mean viscous power dissipation). Using an unconstrained optimization approach, we compute optima starting from 30–50 random initializations across several decades of Pe , the energy budget parameter. At Pe between $10^{4.5}$ and $10^{4.75}$, convective rolls with U-shaped branching near the walls emerge. They exceed the heat transfer of the simple convective roll optimum at Pe between 10^5 and $10^{5.25}$. At larger Pe , multiple layers of branching occur in the optima and become increasingly elongated, asymmetrical, and heterogeneous. The rate of heat transfer scales as $Pe^{0.575}$, which, in this range of Pe , is very close to the $Pe^{2/3}(\ln Pe)^{-4/3}$ behavior of self-similar branching solutions proposed earlier. Compared to the simple convective roll, the branching flows have lower maximum speeds and thinner boundary layers but nearly the same maximum power density.

DOI: [10.1103/PhysRevFluids.8.074502](https://doi.org/10.1103/PhysRevFluids.8.074502)

I. INTRODUCTION

The transfer of heat between solid surfaces and adjacent fluid flows is essential to many natural and technological phenomena [1–4]. Fundamental results in the field of heat transfer concern how the rate of heat transfer (quantified by the Nusselt number Nu) depends on the form of the fluid flow, with the flow magnitude quantified by the Rayleigh number (for buoyancy-driven or free convection) or the Péclet number, Pe (for forced convection) [2,5]. Scaling laws have been derived for fluid flows that are simple in form (e.g., Poiseuille flow through a channel [6]) or flows driven by simple forcings (e.g., pressure-driven flows past obstacles [2,7–9] and buoyancy-driven flows between surfaces at fixed temperatures [10–16]).

Recently, Hassanzadeh *et al.* studied convective flows in a 2D fluid layer between horizontal walls at fixed temperatures, hot at the bottom and cold at the top, as in Rayleigh-Bénard convection [17]. Instead of buoyancy-driven flows, they considered forced incompressible flows and performed a continuation search for flows that maximize the rate of heat transfer from the solid surfaces for a given mean kinetic energy or rate of viscous dissipation of the flow (given as a type of Péclet number). They did not explicitly identify such flows as forced flows, but any incompressible flow is a solution to the Navier-Stokes equation with a given distribution of forcing per unit volume, spread over the flow region [18,19]. They studied steady 2D flows, periodic in the horizontal direction (along the walls), with free-slip boundary conditions. They found optimal flows in the form of rectangular convection rolls of decreasing horizontal width and sharpening boundary layers near the walls as the average input power (Pe) increases. Later, Souza *et al.* performed a continuation search in the fixed-viscous-dissipation case with no-slip instead of free-slip boundary conditions at high Pe with higher numerical resolution and obtained $Nu \sim Pe^{6/11}$ instead of $Pe^{10/17}$ in the free-slip case [20]. Tobasco and Doering analytically constructed self-similar branching flows that obtain

*alben@umich.edu

$\text{Nu} \sim \text{Pe}^{2/3}/(\ln \text{Pe})^{4/3}$ [21,22], close to the $O(\text{Pe}^{2/3})$ upper bound obtained using the background method [23], which holds independently of the flow boundary conditions. Meanwhile, Motoki *et al.* studied the same problem in three dimensions, periodic in the two directions perpendicular to the walls [24]. Both Souza *et al.* and Motoki *et al.* used combinations of Newton's method and artificial time-stepping procedures to solve the system of nonlinear equations obtained by taking variations of the Lagrangian function for the heat transfer with Lagrange multipliers for the constraints of flow incompressibility, the advection-diffusion equation, and the fixed rate of viscous dissipation. At $\text{Pe} = 79.2$, the optimal flows of [24] bifurcate from the 2D rolls of Ref. [20] to 3D flows that eventually adopt branching structures near the no-slip walls. The branching occurs over a wider range of spatial scales as Pe increases from 500 to 10 000. Along with the 3D branching structures, the scaling $\text{Nu} \sim \text{Pe}^{2/3}$ was found. The same method was used earlier by the same authors to study similar transitions with Couette-flow (moving-wall) boundary conditions [25]. Recently, Kumar theoretically constructed 3D branching flows that achieve the scaling $\text{Nu} \sim \text{Pe}^{2/3}$ [26].

The goal of this paper is to search broadly for optimal 2D no-slip flows. Reference [20] found a sequence of rectangular convective rolls as Pe was increased, while Refs. [21,22] constructed a self-similar branching flow that is close to optimal in the large- Pe limit. Are there optimal flows that interpolate between these two, and are there other types of optimal flows? Is there a succession of branching flows similar to those found in 3D by Ref. [24]? We address these questions with a different computational method than the previous works, simpler in some ways because it uses an unconstrained optimization formulation.

II. MODEL

A layer of fluid is contained between walls at $y = 0$ and 1, with temperatures 1 and 0, respectively. We have chosen to nondimensionalize all quantities with dimensions of length (including y) by the channel height H and quantities with units of temperature by the temperature difference between the walls ΔT . We search for a steady 2D flow field $(u, v) = \mathbf{u} = (\partial_y \psi, -\partial_x \psi)$, automatically incompressible for a given stream function $\psi(x, y)$. The flow is assumed periodic in x with period L_x , to be determined as part of the optimization of ψ . The flow velocity is zero at the walls: $\psi = \partial_y \psi = 0$ at $y = 0$ and $\psi = \psi_{\text{top}}$ and $\partial_y \psi = 0$ at $y = 1$. The constant ψ_{top} is the net horizontal fluid flux through the channel. In test runs, our computational solutions always converge to the case $\psi_{\text{top}} = 0$, so we assume this value in general because it reduces the number of optimization parameters.

The temperature field is determined by the steady advection-diffusion equation:

$$\mathbf{u} \cdot \nabla T - \nabla^2 T = 0. \quad (1)$$

We have set the prefactor of $\nabla^2 T$ (the thermal diffusivity) to unity, corresponding to nondimensionalizing velocities by κ/H , with κ the dimensional thermal diffusivity. The setup is similar to Rayleigh-Bénard convection, but instead of solving the Boussinesq equations for the flow field, we determine the flow field that maximizes the Nusselt number, the mean heat transfer from the hot lower boundary:

$$\text{Nu} \equiv \frac{1}{L_x} \int_0^{L_x} -\partial_y T|_{y=0} dx. \quad (2)$$

We maximize Nu over flows with a given spatially averaged rate of viscous dissipation Pe^2 :

$$\text{Pe}^2 \equiv \frac{1}{2} \frac{1}{L_x} \int_0^{L_x} \int_0^1 (\nabla \mathbf{u} + \nabla \mathbf{u}^T)^2 dy dx = \frac{1}{L_x} \int_0^{L_x} \int_0^1 (\nabla^2 \psi)^2 dy dx. \quad (3)$$

Pe^2 is the average rate of viscous dissipation nondimensionalized by $\mu\kappa^2/H^4$, with μ the viscosity. The second equality in Eq. (3) holds for incompressible flows given the no-slip and periodic boundary conditions we have here [27,28].

One way to solve this constrained optimization problem is to find stationary points of the Lagrangian [17,20,24], which can be written as [18,19]

$$\begin{aligned} \mathcal{L} = & \frac{1}{L_x} \int_0^{L_x} -\partial_y T|_{y=0} dx + \frac{1}{L_x} \int_0^{L_x} \int_0^1 m(x, y)(-\nabla^\perp \psi \cdot \nabla T - \nabla^2 T) dy dx \\ & + \lambda \left(\text{Pe}^2 - \frac{1}{L_x} \int_0^{L_x} \int_0^1 (\nabla^2 \psi)^2 dy dx \right). \end{aligned} \quad (4)$$

By setting the variations of \mathcal{L} with respect to T , ψ , and the Lagrange multipliers m and λ to 0 and integrating by parts, we obtain a system of nonlinear equations and boundary conditions for these four variables that can be solved using Newton's method [18]:

$$\frac{\delta \mathcal{L}}{\delta m} = -\nabla^\perp \psi \cdot \nabla T - \nabla^2 T = 0, \quad (5)$$

$$\frac{\delta \mathcal{L}}{\delta T} = \nabla^\perp \psi \cdot \nabla m - \nabla^2 m = 0, \quad (6)$$

$$\frac{\delta \mathcal{L}}{\delta \psi} = \nabla^\perp m \cdot \nabla T + 2\lambda \nabla^4 \psi = 0, \quad (7)$$

$$\frac{\delta \mathcal{L}}{\delta \lambda} = \text{Pe}^2 - \frac{1}{L_x} \int_0^{L_x} \int_0^1 (\nabla^2 \psi)^2 dx dy = 0. \quad (8)$$

The boundary conditions for T and ψ have been stated, and those for m are the same as those for T . In the limit of small Pe , the solutions can be expanded in powers of Pe :

$$T = \mathcal{T}_0 + \text{Pe} \mathcal{T}_1 + \dots, \quad (9)$$

$$m = m_0 + \text{Pe} m_1 + \dots, \quad (10)$$

$$\psi = \text{Pe} \psi_1 + \dots, \quad (11)$$

with $m_0 = \mathcal{T}_0 = 1 - y$, the purely conductive solution. Inserting the expansions into Eqs. (5)–(8), we find $m_1 = -\mathcal{T}_1$ and the system is reduced to a generalized eigenvalue problem:

$$\partial_x \psi_1 - \nabla^2 \mathcal{T}_1 = 0, \quad (12)$$

$$-\partial_x \mathcal{T}_1 - \lambda \nabla^4 \psi_1 = 0. \quad (13)$$

The eigenmodes can be written as $(T_1, \psi_1) = (\hat{\mathcal{T}}_{1k}(y) \sin(kx + \phi), \hat{\psi}_{1k}(y) \cos(kx + \phi))$ for any real k and an arbitrary phase angle ϕ . In Appendix A, we derive an alternative expression for Nu [17]:

$$\text{Nu} = 1 + \frac{1}{L_x} \int_0^1 \int_0^{L_x} vT dx dy, \quad (14)$$

which can be computed using \mathcal{T}_1 and ψ_1 , whereas Eq. (2) would require us to also compute \mathcal{T}_2 , the $O(\text{Pe}^2)$ contribution to T , because $\text{Nu} = 1 + O(\text{Pe}^2)$, and the $O(\text{Pe}^2)$ term determines the optimal flows. We have

$$\text{Nu} = 1 + \frac{1}{2} \int_0^1 k \hat{\psi}_{1k}(y) \hat{\mathcal{T}}_{1k}(y) dy. \quad (15)$$

Two examples of eigenmodes are shown in Figs. 1(a)–1(d). The flows consist of discrete sequences of convective rolls between the two walls, similar to those in Ref. [17], but nonsinusoidal in y now due to the no-slip instead of free-slip boundary condition. The cases with one and two rolls between the walls are shown in Figs. 1(a) and 1(b), and the horizontal period $L_x = 2\pi/k$ is chosen in each case to maximize Nu . Thus, ψ_A and ψ_B are the best and second-best locally optimal flows at $\text{Pe} \ll 1$, and the convective rolls are slightly larger horizontally than vertically. In Figs. 1(c) and

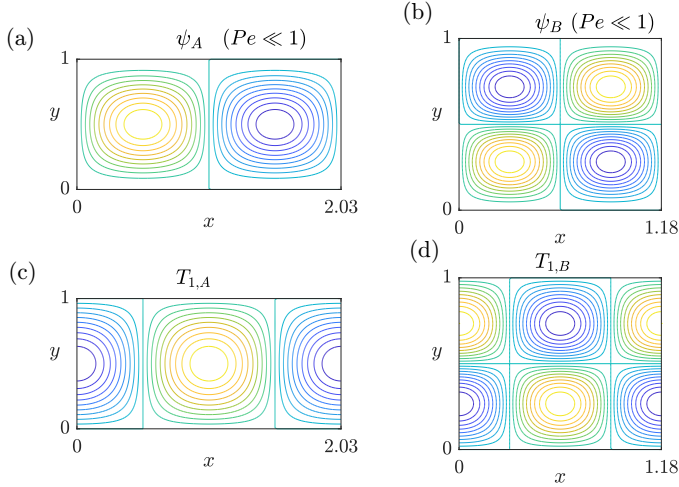


FIG. 1. Streamlines for the best and second-best optimal flows in the limit $Pe \rightarrow 0$ (a), (b) and contour lines for the $O(Pe)$ components of the corresponding temperature fields (c), (d).

1(d), the $O(Pe)$ components of the temperature fields are shifted by $1/4$ period from ψ [in Figs. 1(a) and 1(b)], so there is a local maximum/minimum of temperature where the flow is directed vertically upward/downward between the plates.

References [20,24] solved alternative versions of the variational eqs. (5)–(8), using \mathbf{u} and the pressure p instead of ψ , and found optimal flows at large Pe . The system of equations (5)–(8) involves fourth-order derivatives of ψ , and is ill-conditioned when discretized with finite differences on a fine mesh. To compute solutions at larger Pe , here we adopt an alternative approach that leads to an unconstrained optimization problem.

III. COMPUTATIONAL METHOD

We now describe our computational method to find optimal flows at moderate and large Pe . We include L_x among the optimization parameters by changing variables from x to $p = x/L_x$, so the equations are solved on the fixed domain $p \in [0, 1]$ and Eqs. (1)–(3) become

$$\frac{1}{L_x} (\partial_y \psi \partial_p T - \partial_p \psi \partial_y T) - \left(\frac{1}{L_x^2} \partial_p^2 + \partial_y^2 \right) T = 0 \quad L_x \equiv s^2, \quad (16)$$

$$\text{Nu} = \int_0^1 -\partial_y T|_{y=0} dp, \quad (17)$$

$$\text{Pe}^2 = \int_0^1 \int_0^1 \left(\frac{1}{L_x^2} \partial_p^2 \psi + \partial_y^2 \psi \right)^2 dp dy. \quad (18)$$

We optimize $L_x \equiv s^2$ by using s as the optimization parameter, so L_x is nonnegative while s is unconstrained. Next, we express ψ as a linear combination of functions with period p that satisfy the no-slip boundary conditions in y . The functions are products of Fourier modes in p and linear combinations of Chebyshev polynomials in y :

$$\psi(p, y) = \sum_{j=1}^M \sum_{k=1}^{N-3} A_{jk} Y_k(y) \cos(2\pi j p) + B_{jk} Y_k(y) \sin(2\pi j p), \quad (19)$$

$$Y_k(y) \in \langle T_0(2y-1), \dots, T_{k+4}(2y-1) \rangle. \quad (20)$$

Y_k is a linear combination of Chebyshev polynomials of the first kind up to degree $k + 4$ that obeys the no-slip conditions at $y = 0$ and 1. Its computation is described in Appendix B. An arbitrary horizontal shift can be added to ψ without changing the solution. To remove this degree of freedom, we set $B_{11} = 0$.

We define a grid that is uniform in p with $m = 256$ points, $\{0, 1/m, \dots, 1 - 1/m\}$. We concentrate points near the boundaries in y , anticipating sharp boundary layers in the optimal flows. This is done by starting with a uniform grid for $\eta \in [0, 1]$ with spacing $1/n$, and mapping to the y grid by

$$y = \eta - \frac{y_f}{2\pi} \sin(2\pi\eta). \quad (21)$$

with y_f a scalar. The y spacing is maximum, $\approx (1 + y_f)/n$, near $y = 1/2$, and minimum, $\approx (1 - y_f)/n$, near $y = 0$ and 1. We take $y_f = 0.997$ and $n = 512$ or 1024, giving a grid spacing $\Delta y \approx 3 \times 10^{-6}$ or 6×10^{-6} at the boundaries.

The discretized ψ is written Ψ , a vector of values at the $m(n - 1)$ interior mesh points for $(p, y) \in [0, 1) \times (0, 1)$. To form Ψ , we first normalize each mode in Eq. (19) to have power Pe^2 (for better numerical conditioning). The differential operators and the integrals in Eq. (18) are discretized to compute the power with second-order accuracy. We arrange the modes as columns of a $m(n - 1) \times 2M(N - 3) - 1$ matrix \mathbf{V} . Here we take $M = 5m/32$ and $N = 5n/32$, so we limit the modes to those whose oscillations can be resolved by the mesh. We set $\tilde{\Psi} = \mathbf{V}\mathbf{c}$, a linear combination of the discretized modes with coefficients \mathbf{c} . To form a Ψ with power Pe^2 , we discretize the integral in Eq. (18) as a quadratic form $\mathbf{a}^T \mathbf{M}\mathbf{a}$, where the vector \mathbf{a} stands for a discretized ψ in Eq. (18), and the matrix \mathbf{M} gives the effect of the discretized derivatives and integrals in Eq. (18). Then

$$\Psi = \frac{\text{Pe Vc}}{\sqrt{(\mathbf{Vc})^T \mathbf{M} \mathbf{Vc}}} \quad (22)$$

has power Pe^2 , as can be seen by evaluating $\Psi^T \mathbf{M} \Psi$. Such a Ψ automatically gives an incompressible flow by the stream function definition, and automatically satisfies the power constraint, so we are left with an unconstrained optimization problem: maximize Nu [Eq. (17), discretized at second order] over $\mathbf{c} \in \mathbb{R}^{2M(N-3)-1}$ and $s \in \mathbb{R}$.

We solve the optimization problem using the Broyden-Fletcher-Goldfarb-Shanno (BFGS) method [29], a quasi-Newton method that requires evaluations of the objective function Nu and its gradient with respect to the design parameters: $\{d\text{Nu}/d\mathbf{c}, d\text{Nu}/ds\}$. Nu is computed by forming Ψ from \mathbf{c} , then computing \mathbf{u} and solving Eq. (16) for the discretized temperature field \mathbf{T} using second-order finite differences. We use a second-order rather than spectral discretization to obtain a sparse matrix in the advection-diffusion equation, allowing for relatively fast solutions.

The gradient can be computed efficiently using the adjoint method [29]. Using the chain rule,

$$\frac{d\text{Nu}}{d\mathbf{c}} = \frac{d\text{Nu}}{d\mathbf{T}} \frac{d\mathbf{T}}{d\Psi} \frac{d\Psi}{d\mathbf{c}}; \quad \frac{d\text{Nu}}{dL_x} = \frac{d\text{Nu}}{d\mathbf{T}} \frac{d\mathbf{T}}{dL_x} + \frac{d\text{Nu}}{d\mathbf{T}} \frac{d\mathbf{T}}{d\Psi} \frac{d\Psi}{dL_x}. \quad (23)$$

The right-hand side of the second of Eqs. (23) is a sum of two terms because \mathbf{T} depends on L_x directly, through the coefficients of Eq. (16), and through Ψ , which depends on L_x through \mathbf{M} in the denominator of Eq. (22). In the first of Eqs. (23), \mathbf{T} depends on \mathbf{c} only through Ψ .

The entries of $d\mathbf{T}/d\Psi$ and $d\mathbf{T}/dL_x$ can be calculated using the discretized advection-diffusion equation (16), written as

$$\mathbf{r}(\mathbf{T}, \Psi, L_x) = 0 \quad (24)$$

with \mathbf{r} (the residual) a vector that takes values at each interior grid point. We can think of Eq. (24) as an implicit equation for the temperature field \mathbf{T} as a function of Ψ and L_x . If we apply small perturbations $(\Delta\Psi, \Delta L_x)$ to Ψ and L_x , we obtain a small perturbation $\Delta\mathbf{T}$ to the temperature field such that the residual remains zero:

$$0 = \Delta\mathbf{r} \approx \frac{d\mathbf{r}}{d\mathbf{T}} \Delta\mathbf{T} + \frac{d\mathbf{r}}{d\Psi} \Delta\Psi + \frac{d\mathbf{r}}{dL_x} \Delta L_x. \quad (25)$$

In the limits $\|\Delta\Psi\| \rightarrow 0$ and $\|\Delta L_x\| \rightarrow 0$, the matrices that map $\Delta\Psi$ and ΔL_x to $\Delta\mathbf{T}$ are

$$\frac{d\mathbf{T}}{d\Psi} = -\frac{d\mathbf{r}^{-1}}{d\mathbf{T}} \frac{d\mathbf{r}}{d\Psi}; \quad \frac{d\mathbf{T}}{dL_x} = -\frac{d\mathbf{r}^{-1}}{d\mathbf{T}} \frac{d\mathbf{r}}{dL_x}, \quad (26)$$

so Eqs. (23) become

$$\frac{d\text{Nu}}{d\mathbf{c}} = -\frac{d\text{Nu}}{d\mathbf{T}} \frac{d\mathbf{r}^{-1}}{d\mathbf{T}} \frac{d\mathbf{r}}{d\Psi} \frac{d\Psi}{d\mathbf{c}} = -\mathbf{q}^T \frac{d\mathbf{r}}{d\Psi} \frac{d\Psi}{d\mathbf{c}}; \quad \frac{d\text{Nu}}{dL_x} = -\mathbf{q}^T \frac{d\mathbf{r}}{dL_x} - \mathbf{q}^T \frac{d\mathbf{r}}{d\Psi} \frac{d\Psi}{dL_x}. \quad (27)$$

where \mathbf{q} is the adjoint variable and is computed by solving the adjoint equation:

$$\frac{d\mathbf{r}^T}{d\mathbf{T}} \mathbf{q} = \frac{d\text{Nu}^T}{d\mathbf{T}}. \quad (28)$$

Here $d\mathbf{r}/d\mathbf{T}$ is a sparse matrix that corresponds to the differential operators that multiply T in (16), discretized with second-order finite differences. The cost of solving the linear system Eq. (28) for \mathbf{q} , and therefore the cost of computing the gradient terms $\{d\text{Nu}/d\mathbf{c}, d\text{Nu}/dL_x\}$, is essentially the same as that of computing Nu itself, by solving Eqs. (16) and (17). As noted above, we optimize over s instead of L_x to ensure $L_x \geq 0$, and use $d\text{Nu}/ds = 2s d\text{Nu}/dL_x$ instead of $d\text{Nu}/dL_x$ for the gradient.

We initialize with 30–50 random choices of \mathbf{c} and s and run the optimization until convergence, when $\|(d\text{Nu}/d\mathbf{c}, d\text{Nu}/ds)\|$ is less than a threshold that ranges from 10^{-8} to 10^{-2} . Larger thresholds are allowed at larger Pe, where the gradient is larger in the initial random state, and where convergence to very small gradients is more difficult. At large Pe, the initial gradient norm is typically between 10^3 and 10^4 , so the gradient norm threshold of 10^{-2} corresponds to 10^{-5} – 10^{-6} relative to the initial norm. The discretized advection-diffusion equation becomes increasingly ill-conditioned as Pe increases, causing a decrease of accuracy in Nu and its gradient, and slowing convergence [30]. Nonetheless, we are able to obtain accurate Nu values up to $\text{Pe} = 10^{7.5}$.

IV. COMPUTATIONAL RESULTS

In Fig. 2, we show the progression of optimal flows and corresponding temperature fields as Pe increases from $10^{1.5}$. Here the temperature field is the whole temperature field, not just the deviation from the conductive part as in Fig. 1. At $\text{Pe} = 10^{1.5}$, the convective rolls are very close to those for $\text{Pe} \ll 1$ in Fig. 1(a), and the local increase in the temperature where the flow is upward from the hot lower boundary at the x midpoint can be seen.

As Pe increases to $10^{4.5}$, the convective rolls become narrower horizontally, increasing the surface area where hot upwelling regions meet cold downwelling regions. The advantage for heat exchange is sufficient to outweigh the increase in viscous power dissipation due to the increase in $|\partial_x v|$ with convective roll narrowing. The viscous power dissipation is largest along the boundary, where $|\partial_y u|$ is particularly large. The best optimal flows are labeled ψ_A and are the same as those in Ref. [20]. At $\text{Pe} = 10^{3.5}$ and above, small closed streamlines emerge close to the boundaries, showing a region of concentrated flow there. Despite this additional complexity, we refer to the flows labeled ψ_A collectively as simple roll optima, in contrast to the alternative flow optima we show next. In four cases, optima that are slight variations of the simple roll optima are shown, labeled ψ_B . At $\text{Pe} = 10^{2.5}$, the two convective rolls for ψ_B are noticeably asymmetrical, while at $\text{Pe} = 10^{3.5}$ and above the two rolls are skewed in oblique directions. In these latter cases, we will show that there is little change in Nu ($\lesssim 1\%$), so the skewed convective rolls are almost as efficient as the straight, simple rolls.

Between $\text{Pe} = 10^{4.5}$ and 10^5 , the class of optima changes dramatically with the emergence of branched flows. Examples of the best local optima at $\text{Pe} = 10^5$ are shown in Fig. 3. Each flow is shown by three panels, a tall narrow panel showing the streamlines over the whole domain, and to its right, two wider panels showing the streamlines close to the boundaries (within distance 0.15). The flows are labeled at the top with their Nu value. Flow A, with $\text{Nu} = 100$, is the simple convective roll optimum and is the global optimum. (In this paper, “global optimum” means the best optimum

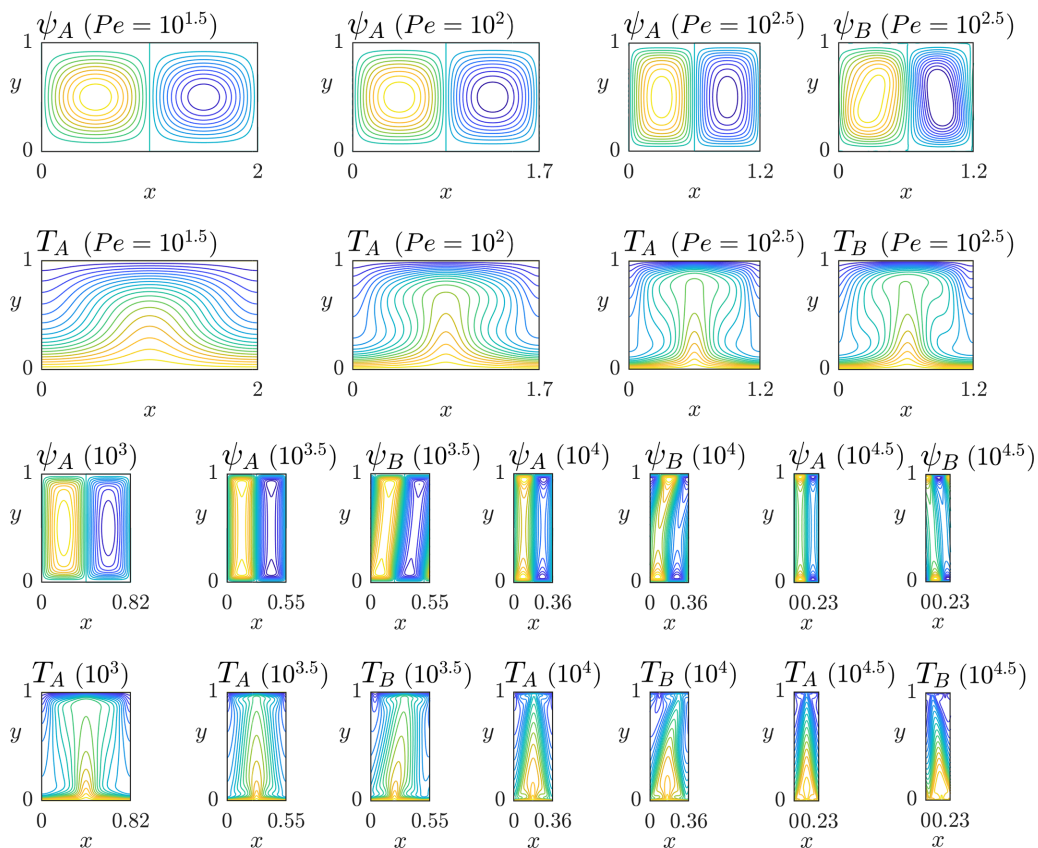


FIG. 2. The progression of optimal flows and temperature fields as Pe increases from $10^{1.5}$ to $10^{4.5}$. Shown are the best flow and temperature fields among the optima, (ψ_A, T_A) , and at four Pe an alternative optimum (ψ_B, T_B) with the temperature field below the corresponding flow.

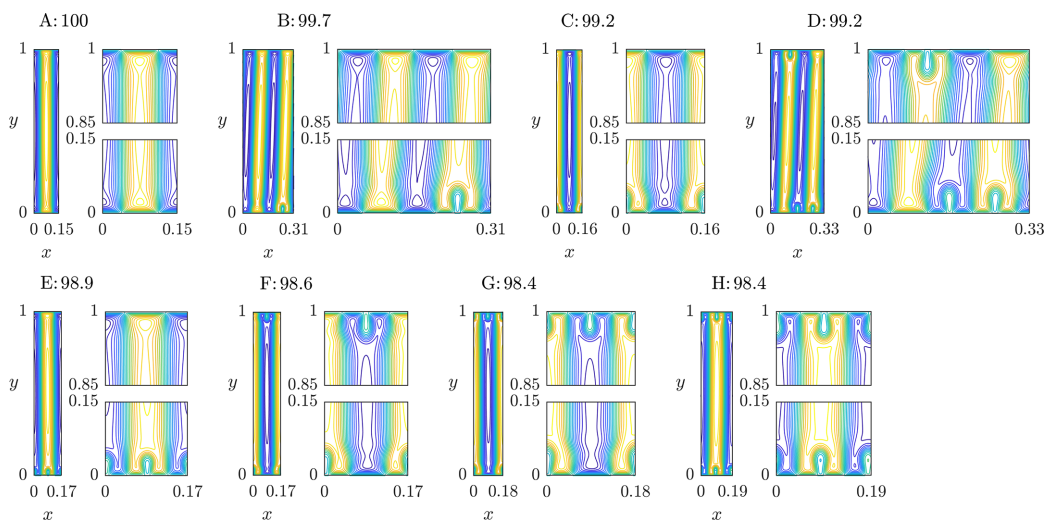
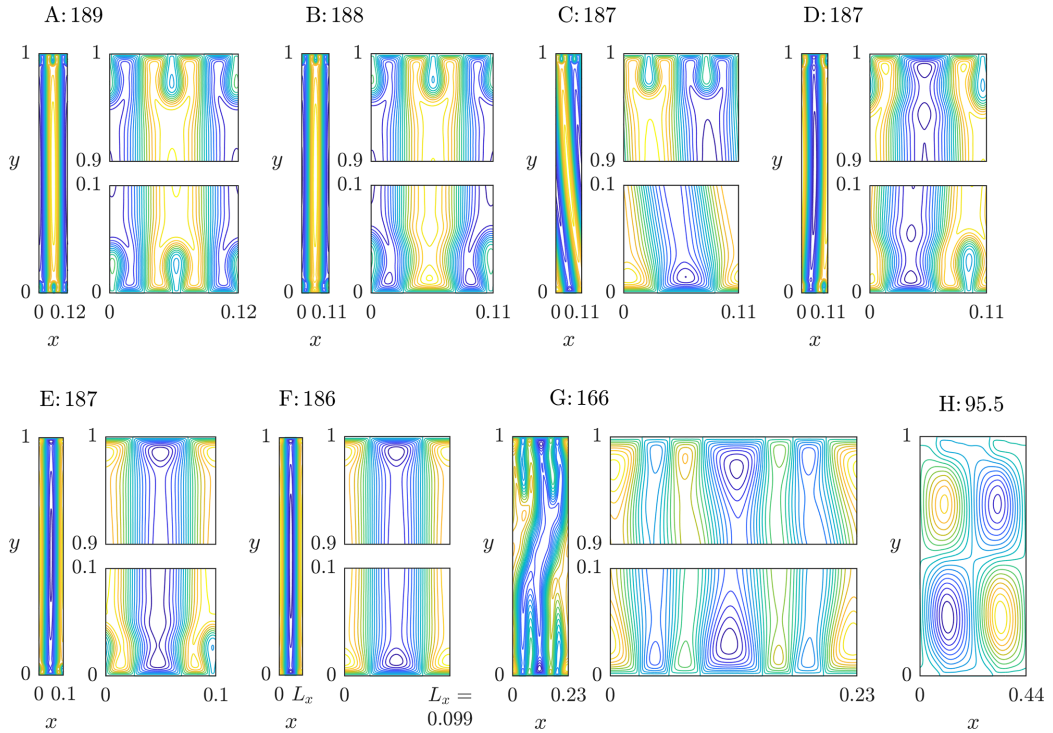


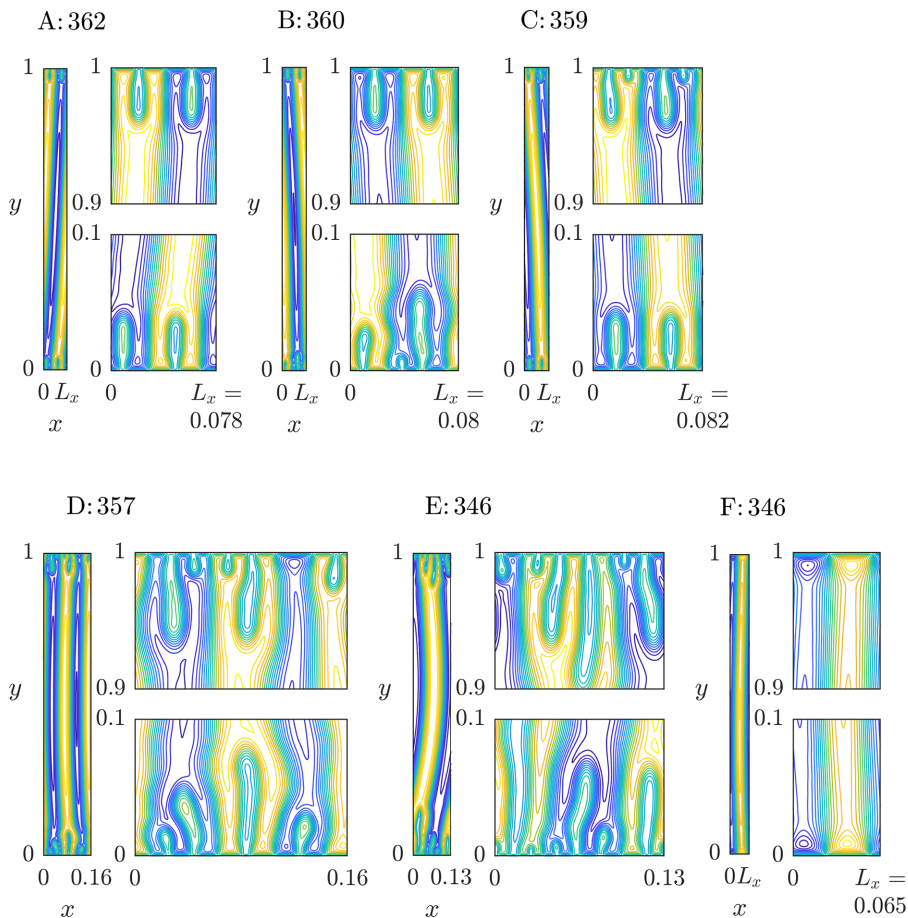
FIG. 3. Optimal flow fields at $Pe = 10^5$.


 FIG. 4. Optimal flow fields at $Pe = 10^{5.5}$.

among those we have computed, not among all possible flows, which cannot be determined by computations like these). Flow B has two pairs of convective rolls, and one of the eight roll ends shows a branched structure near the bottom boundary. The flow is noticeably skewed, but by many comparisons of other examples of skewed and nonskewed optima, the skewness seems to have little effect on Nu . In flows C–H, the proportion of branched ends generally increases while Nu decreases, with some ties between neighboring flows. There are additional versions of these flows (not shown) with variations in the degree of skewness.

Optimal flows for $Pe = 10^{5.5}$, shown in Fig. 4, are similar, with slightly elongated branched regions compared to $Pe = 10^5$. Now the globally optimal flow (A) has branched ends. Moving from A to F, Nu decreases while the number of branched ends also decreases, the reverse trend of Fig. 3. The simple roll optimum is F with $Nu = 186$, within 2% of the global optimum, 189 (A). Optima G and H have much lower Nu , but are shown to illustrate the wide range of optima that may occur, including cases like G with branching but with Nu well below the global optimum. No inset is shown for H because the flow lacks fine structures near the walls and is surprisingly similar to the second best optimum for $Pe \ll 1$ [Fig. 1(b)]. We hypothesize that G and H are just a small sample of a much larger space of optima with much lower Nu . The algorithm tends to find Nu close to the maximum in most cases, however, because at each iterative step, a backtracking line search in the direction of the gradient is used, and it accepts a step when it gives a flow with higher Nu . As a result, the algorithm probably tends to wander away from local optima with relatively small Nu , such as G and H.

Figure 5 shows optimal flows at $Pe = 10^6$. The branched tips are more elongated now, and small recirculation regions with closed streamlines are seen at their tips, similar to the simple roll optimum (flow F, with $Nu = 346$). There is also more skewness in the flows here, a general trend as Pe increases. Flows B–D have branched tips that undergo a second level of branching, a step towards

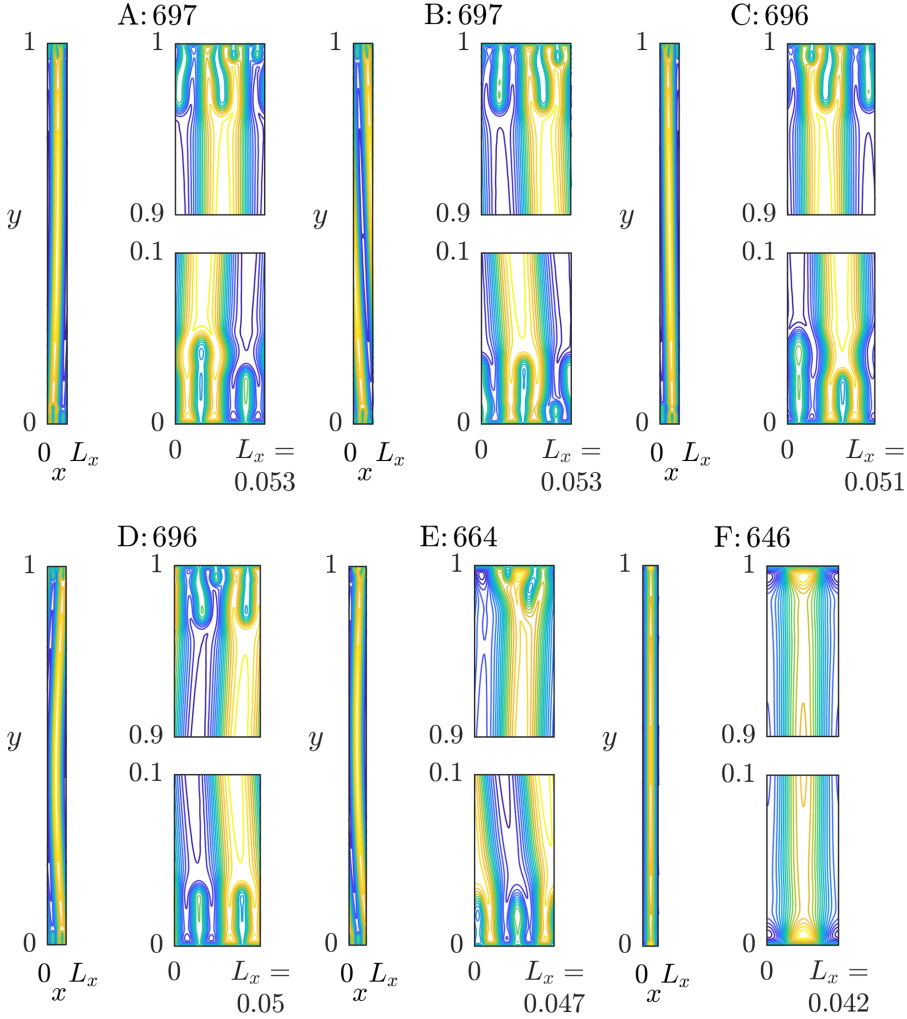

 FIG. 5. Optimal flow fields at $Pe = 10^6$.

the hierarchical branching flows of Ref. [21]. Flow E is a case with three levels of branching near the top boundary. Although these flows are local optima, Nu decreases with the complexity of the branched structures, though there is also an increased gap between Nu for the global optimum (A), which has branching, relative to the simple roll optimum (F), with no branching.

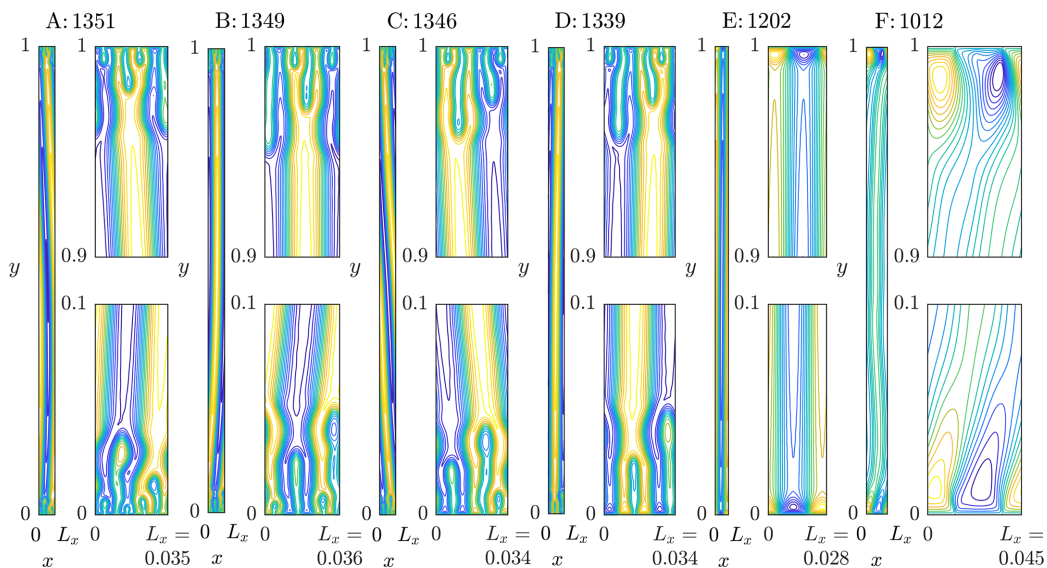
With Pe increased further, to $10^{6.5}$, Fig. 6 shows a continuation of many of the same trends. Now the global optimum has two layers of branching. In all cases, there is further elongation of the branched tips, which also adopt more complex shapes, with changes in width and direction near the walls (e.g., near the top walls in C and E). There is a steady decrease in the optimal L_x with increasing Pe , which was identified with a power-law behavior in Ref. [20] for the simple roll optimum.

At $Pe = 10^7$ (Fig. 7), the optimal flows (A–D) still have two layers of branching in some cases, but with increased elongation and waviness in the boundaries of the branches. The increase in Nu in flows A–D over that of the simple roll optimum (E) now exceeds 10%. Flow F is an optimum with much lower Nu that resembles a skewed version of the simple convective roll. It also has larger and stronger eddies close to the walls, with less extreme values of the stream function in the interior, and therefore a weaker wall-to-wall flow.

At the largest Nu studied here, $Pe = 10^{7.5}$, the flows again have one or two levels of branching and further elongation of the branches (Fig. 8). It is possible that the simultaneous optimization of


 FIG. 6. Optimal flow fields at $Pe = 10^{6.5}$.

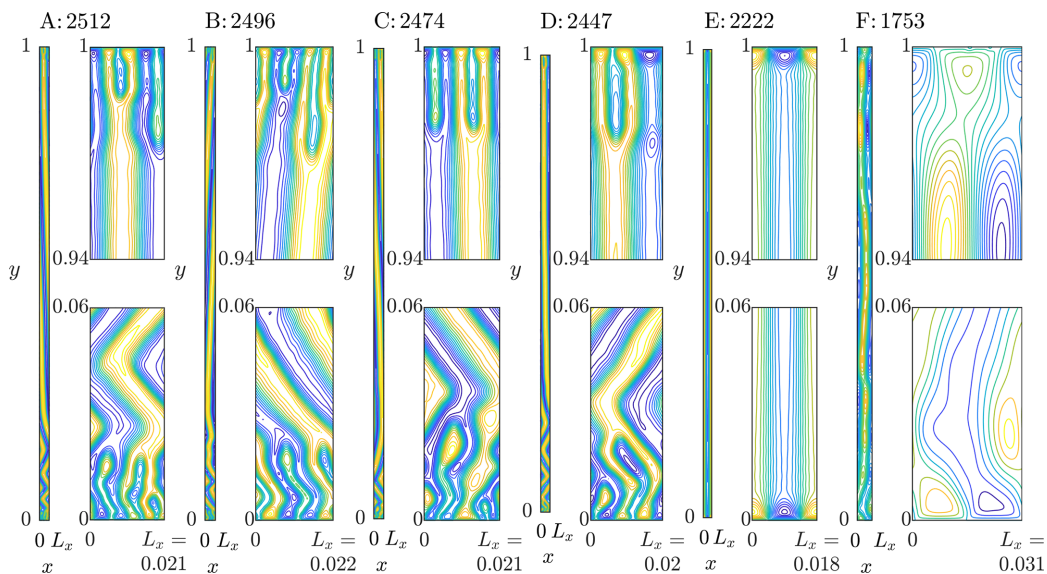
L_x and the flow inhibits the appearance of higher levels of branching, which would require larger L_x . Near the bottom boundary, flow C has three levels of very wavy branches shown by the blue streamlines (which can be seen by following the streamlines across the periodic boundary). There is generally a peculiar waviness of the flows near the bottom boundary. There is no asymmetry between the top and bottom boundaries in the model and no obvious asymmetry in the computations, except in the ordering of the unknowns for the matrix equations, i.e., Eq. (16) for \mathbf{T} and Eq. (28) for \mathbf{q} . The unknowns are ordered starting at the lower left corner and proceeding rightward across a horizontal row and then upward row by row. We have not investigated the effect of the ordering of unknowns, but given that the discrete advection-diffusion operator becomes increasingly ill-conditioned as Pe increases, the solutions will eventually become noticeably inaccurate, and the waviness could be an early indication of this effect. Although we do not understand the reason for the up-down flow asymmetry at the largest Pe ($10^{7.5}$), we have checked that the heat transfer for these flows is converged with respect to further increases in mesh spacing. The changes in Nu when doubling the mesh in either direction are much less than 1% for the optimal flows at $Pe \leq 10^{6.5}$ and between 1 and 2% at $Pe = 10^7$ and $10^{7.5}$.


 FIG. 7. Optimal flow fields at $Pe = 10^7$.

Flow F is an example of an atypical optimum, with strong eddies distributed away from the walls and throughout the domain, and no branching near the walls.

In Fig. 9, we plot Nu for the flows shown thus far, and additional computed flows that were not shown. The simple roll optima Nu are shown with red hash marks centered at the corresponding (Pe, Nu) pair. The values for the four alternative flows in Fig. 2 are shown by the blue triangles. The values for the alternative flows above the branching transition (for $Pe \geq 10^{4.75}$) are shown by the black hash marks, which can exceed Nu for the red hash marks for $Pe \geq 10^{5.25}$.

The simple convective roll solutions (red hash marks) fit $Nu \sim Pe^{0.54}$ (red dashed dotted line above), the same as in Ref. [20]. The upper envelope of the black marks, which correspond to


 FIG. 8. Optimal flow fields at $Pe = 10^{7.5}$.

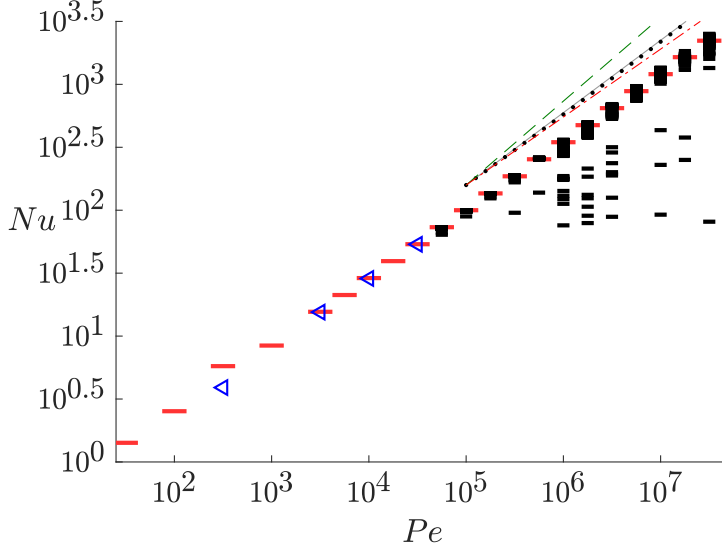


FIG. 9. Nu versus Pe for optimal flow fields shown in this paper and additional computed cases. The red hash marks give Nu for the simple roll optima. The black hash marks give Nu for other optima at $Pe \geq 10^{4.75}$. The blue triangles show Nu for ψ_B, T_B in Fig. 2. The lines at the upper right correspond to the trends $Nu \sim Pe^{2/3}$ (green dashed line), $Pe^{2/3}(\ln Pe)^{-4/3}$ (black dotted line), $Pe^{0.575}$ (gray solid line), and $Pe^{0.54}$ (red dashed dotted line), from top to bottom. The black dotted line and gray solid line almost coincide.

certain branching flow optima, has a maximum slope of 0.575 (gray solid line above), very close to $Nu \sim Pe^{2/3}(\ln Pe)^{-4/3}$ (the black dotted line that almost coincides with the gray solid line) of the self-similar 2D branching flows of [21]. All these trends are well below the $Pe^{2/3}$ upper bound (green dashed line) [23] that has been seen in 3D computationally [24] and theoretically [26], but not in the 2D problem studied here. At the upper end of the Pe range considered here, 10^7 – $10^{7.5}$, the slope of the upper envelope of the black hash marks drops from 0.575 to slightly below 0.54, indicating perhaps that the computations are less successful in approximating globally optimal flow(s) in this region.

So far, we have presented the streamlines of the optimal flow configurations. The flow speed is proportional to the spacing between the streamlines, but since we limit the streamlines to 21 equally spaced values of the stream function for visibility, this gives only a rough estimate. Also, near the walls the streamlines are too close together to perceive their spacing. For a more accurate view, in Fig. 10 we plot the flow speed as a color field near the top wall for three optima from Fig. 5 (in the top row) and four optima from Fig. 7 (in the bottom row), with labels at the top of each panel identifying the specific flow. In each row, the color bar gives the speeds for all the color fields in that row. At the right, the flow speed versus the vertical coordinate is plotted along one cross section for each panel, shown by the red arrows. The cross section is located at x where the highest speed occurs in the whole flow domain, and the cross-section speed is plotted along the entire range $0 \leq y \leq 1$ even though the color fields are limited to $0.9 \leq y \leq 1$. On the horizontal axis, two separate logarithmic scales are used for $0 < y \leq 1/2$ and $1/2 \leq y < 1$. The data are logarithmically spaced with respect to distance from $y = 0$ on the left half of the plot, and from $y = 1$ on the right half, to show the boundary layers near both walls.

For all seven flows considered here, the highest flow speed occurs at the boundary layer next to one of the walls. We define the boundary layer width δ for each flow as the distance from the flow speed maximum to the nearest wall. For the top row, $Pe = 10^6$, the speeds reach a peak $\approx 2 \times 10^4$ over a boundary layer of width $\approx 10^{-3}$, while in the bottom row, $Pe = 10^7$, the speeds

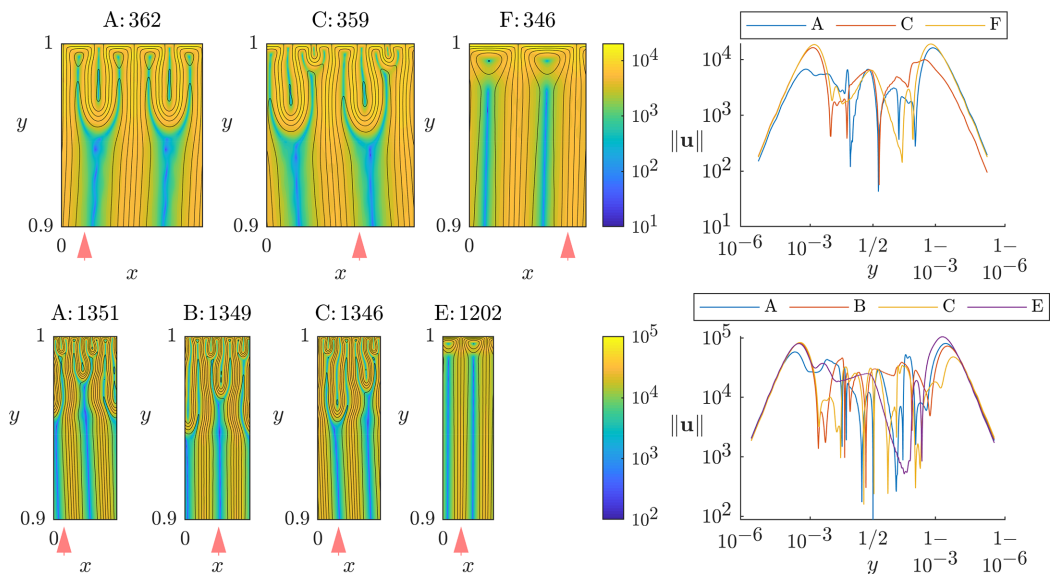


FIG. 10. Color field plots of flow speed overlaid with streamlines (in black) for three optima from Fig. 5 (in the top row) and four optima from Fig. 7 (in the bottom row), with labels at the top of each panel identifying the specific flow. At the right, the flow speed versus the vertical coordinate is plotted along one cross section for each panel, shown by the red arrows.

reach a peak $\approx 10^5$ over a boundary layer of width $\approx 4 \times 10^{-4}$. The peak speeds and boundary layer widths are about 20% higher for the simple convective roll than for the best optimum in the top row (A:362 and F:346) and about 40–60% higher in the bottom row (A:1351 and E:1202), where Pe is larger.

For the simple convective rolls, we find that the maximum speed $\|\mathbf{u}\|_{\max} \sim Pe^{0.75}$ and $\delta \sim Pe^{-0.49}$ for $10^5 \leq Pe \leq 10^{7.5}$. The maximum power density is approximately the wall vorticity squared, $\approx \|\mathbf{u}\|_{\max}^2 / \delta^2 \sim Pe^{2.48}$, and grows faster than the average power density $= Pe^2$. For the optimal flows [(a) panels in Figs. 3–8], we find $\|\mathbf{u}\|_{\max} \sim Pe^{0.71}$ and $\delta \sim Pe^{-0.54}$. Both $\|\mathbf{u}\|_{\max}$ and δ are smaller than for the simple convective roll, but the maximum power density is almost the same and has almost the same scaling with Pe ($\sim Pe^{2.5}$).

Next, we consider the length scales of the main flow structures and how they depend on Pe . In Fig. 11, we plot L_x and lengths of flow features for the simple convective rolls and the branching optima in Figs. 3–8, i.e., over $10^5 \leq Pe \leq 10^{7.5}$. At the top of the figure, the black crosses and red circles give the values of L_x for the branching optima and the simple convective rolls, respectively. The two sets of data are fairly close to each other and to the trend $Pe^{-1/3} (\ln Pe)^{1/6}$ (black solid line) given by Tobasco and Doering [21] for the bulk length scale, i.e., the width of convective rolls far from the walls, in their analytical branching flows. The black crosses do not follow the analytical scaling for branching flows significantly better than the red circles (for flows without branching), but possibly one would see a difference at much larger Pe . Three of the four scattered black crosses above the trend line at $Pe = 10^5$ and 10^6 are for cases in Figs. 3 and 5 that have two pairs of outer convective rolls per horizontal period (L_x), and hence for these cases L_x is roughly double the values of the other cases at these Pe .

Below the red circles are three more data sets giving lengths scales of flow features near the walls for the branching optima only in Figs. 3–8. We identify three types of flow regions adjacent to the walls. Each is defined by a portion of the wall between two flow stagnation points on the wall. Streamlines run from these stagnation points to other stagnation points, typically also located on one of the walls. Examples of all three types of flow regions are seen near the branched end of a

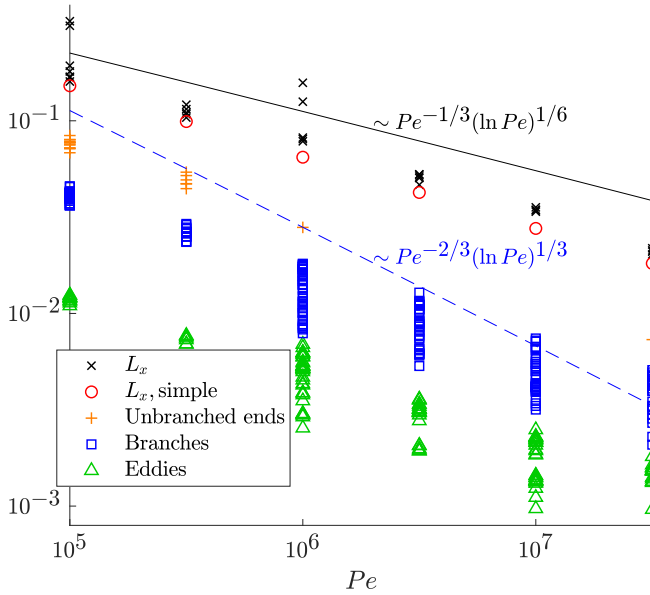


FIG. 11. Dependences of flow length scales on Pe for the simple convective rolls and the branching optima in Figs. 3–8.

convection roll at the bottom of Fig. 3(b). To the left of the branched end is the first type of region, with blue streamlines, which we call an unbranched end. It is bounded by two green streamlines that run from stagnation points at the bottom wall to stagnation points at the top wall. We call the second type of region a branch, exemplified by the two branches on the branched end in Fig. 3(b). They are bounded by one streamline that runs from the bottom wall to the top wall, and a second streamline that runs from the bottom wall to another point on the bottom wall. The region enclosed by this second streamline is the third type of region, which we call an eddy. To summarize, the three regions are defined by portions of the walls that are bounded by two stagnation points. If both streamlines that emanate from the walls at these stagnation points run to the other wall, we have an unbranched end. If one runs to the other wall and the other does not, we have a branch. If both streamlines run to the same wall (and are the same streamline in fact), we have an eddy.

We define the length of each region by the length of the portion of the wall that defines it. This is only an estimate, however. It can be seen in Figs. 3–8 that the widths of branched and unbranched ends and eddies vary as one moves away from the walls. The unbranched ends’ lengths are shown by orange plusses in Fig. 11. These occur most commonly at $Pe = 10^5$ and $10^{5.5}$, where some of convective rolls in the branching optima have unbranched ends, like the simple convective roll. The branches’ lengths are shown by blue squares. They are fairly uniform in length at $Pe = 10^5$ and $10^{5.5}$ and span a much wider range of lengths at $Pe = 10^6$ – $10^{7.5}$, where there are multiple levels of branching. The eddies’ lengths are shown by green triangles. They are smaller than the branches’ lengths, and have a similar transition from greater to lesser uniformity when Pe reaches 10^6 . Tobiasco and Doering defined a boundary layer length scale of $Pe^{-2/3}(\ln Pe)^{1/3}$ (blue dashed line here) for the branches and eddies, which have the same lengths in their analytical construction [21]. The length scales of the branches and eddies in the computed optima cover wide ranges at each Pe here. If we take the mean of the ranges on the log scale as a typical length, they do not seem to decay as quickly as the analytical relationship over this range of Pe . Computations beyond the largest Pe here would help clarify the asymptotic behaviors.

It is also interesting to consider the relative magnitudes of convective transport, $\mathbf{u}T$, and diffusive transport, ∇T . At large Pe we find that convective transport dominates diffusive transport, i.e.,

$\|\mathbf{u}T\| \gg \|\nabla T\|$, except in very thin layers near the walls and in streaks that emanate short distances from the walls, $O(10^{-3})$ at $Pe = 10^6$ and $O(10^{-4})$ at $Pe = 10^7$, along streamlines that emanate from the walls at stagnation points.

V. CONCLUSIONS AND DISCUSSION

We have computed optimal steady flows for heat transfer in a 2D region between parallel walls, the “wall-to-wall” problem [17,20,24]. At $Pe \ll 1$, the optimal flows are squarish convection rolls, similar to the free-slip case [17]. In contrast to previous studies, at large Pe we used an unconstrained optimization method with the adjoint method to compute gradients and the BFGS algorithm to maximize the Nusselt number. Starting from 30–50 random initial flows, and increasing Pe from $10^{1.5}$ to $10^{7.5}$, we find a sequence of transitions. For moderate Pe ($\in [10^{1.5}, 10^{4.5}]$), the algorithm converges to rectangular convection rolls (the “simple convective roll”) or perturbations with skewed convection rolls that have nearly the same Nu as the simple convective roll in most cases.

Between $Pe = 10^{4.5}$ and $10^{4.75}$, optima with branched ends that have a simple U shape become prominent. They have Nu that is less than, but within 2% of, that of the simple convective roll at $Pe = 10^5$. Here Nu decreases with the degree of branching. At $Pe = 10^{5.5}$, Nu instead increases with the degree of branching, and the optimal solution has bilaterally symmetric rolls with U-shaped branched ends. The simple convective roll, without branching, has Nu within 2% of it. Very different optima with much lower Nu are also found, indicating a much larger space of local optima. The simple convective roll and the optima with U-shaped branched ends seem to persist as distinct branches of optima over the range $10^5 \leq Pe \leq 10^{5.5}$, and possibly beyond, though our algorithm is focused on maximizing Nu rather than tracing branches of optima over their maximal ranges of existence.

At $Pe = 10^6$, optima with two and three layers of branching are found, though the best optimum again has a single layer of U-shaped branching at the walls. As Pe increases, there is a general trend towards more vertically elongated branching as well as smaller L_x , perhaps for the same reason—to increase lateral conduction across convective rolls. There is also the presence of small closed eddies at the branched ends, as occurs for the simple convective roll. The branching patterns become more complex and deviate more from symmetry across vertical planes. These trends continue at $Pe = 10^{6.5}$, 10^7 , and $10^{7.5}$.

The scaling exponent for Nu with respect to Pe is as large as 0.575, larger than 0.54 for the simple convective roll, and similar to the $Pe^{2/3}(\ln Pe)^{-4/3}$ behavior of the analytical solutions of [21] in this range of Pe . It is currently unclear if 2D solutions can reach the 2/3 scaling (without logarithmic corrections) that is an upper bound in 2D [23] and is seen in the the 3D computations of Ref. [24] and the 3D analysis of Ref. [26]. We also studied the scaling of the flow speed and boundary layer thickness near the wall, defined as the distance from the wall to the global maximum speed, which always occurs very close to the wall, at the end of a monotonic rise from zero velocity at the wall. For the branched flows, the maximum speed and the boundary layer thickness are both somewhat smaller than for the simple convective roll at the same Pe , and so are the power law exponents. However, the maximum power density, the squared ratio of the maximum speed and boundary layer thickness, is very close in both cases, with scalings close to $Pe^{2.5}$, compared to the Pe^2 spatial average.

Two-dimensionality makes the problem more tractable computationally than the 3D case [24], though this is balanced somewhat by the need to compute at higher Pe to study the branching transition and the asymptotic scaling of Nu with Pe , still unclear at the largest Pe used here, $10^{7.5}$. At larger Pe , the solutions would probably continue to develop more complex branching structures, perhaps with a hierarchy of levels like that in Ref. [21], but probably with more heterogeneity near the boundaries, as seen in the computed optima here. In Ref. [24] a $Nu \sim Pe^{2/3}$ scaling is already clear at $Pe = 10^4$. At higher Pe , the optimal flows and corresponding temperature fields have sharper gradients, which may inhibit the convergence to optimal solutions.

ACKNOWLEDGMENT

This research was supported by the NSF-DMS Applied Mathematics program under Award No. DMS-2204900.

APPENDIX A: OTHER EXPRESSIONS FOR THE NUSSELT NUMBER

Writing Eq. (1) in divergence form and integrating over a horizontal period,

$$0 = \int_0^{L_x} \nabla \cdot (\mathbf{u}T - \nabla T) dx = \int_0^{L_x} \partial_x(uT - \partial_x T) + \partial_y(vT - \partial_y T) dx = \partial_y \int_0^{L_x} (vT - \partial_y T) dx, \quad (\text{A1})$$

using the periodicity of the flow and temperature for the last equality. Thus

$$\frac{1}{L_x} \int_0^{L_x} (vT - \partial_y T) dx \quad (\text{A2})$$

is constant in y . Evaluating Eq. (A2) at $y = 0$ or $y = 1$ (where $v = 0$), we have the rate of heat transfer from the hot boundary or the rate of heat transfer to the cold boundary, both equal to Nu . Integrating Eq. (A2) from $y = 0$ to 1 , we have

$$\text{Nu} = 1 + \frac{1}{L_x} \int_0^1 \int_0^{L_x} vT dx dy. \quad (\text{A3})$$

Reference [21] shows that Nu has a minimum value of 1 for the purely conductive temperature field ($T = 1 - y$) that occurs with $\mathbf{u} = \mathbf{0}$, and is strictly greater than 1 for any other \mathbf{u} (and the corresponding T).

APPENDIX B: NUMERICAL DETAILS

The subspace of $\langle T_0(2y - 1), \dots, T_{k+4}(2y - 1) \rangle$ that obey the no-slip conditions at $y = 0$ and 1 consists of $\sum A_k T_k(2y - 1)$ such that

$$\sum A_k T_k(-1) = \sum (-1)^k A_k = \mathbf{v}_1^T \mathbf{A} = 0, \quad (\text{B1})$$

$$\sum A_k T_k(1) = \sum A_k = \mathbf{v}_2^T \mathbf{A} = 0, \quad (\text{B2})$$

$$\sum A_k T'_k(-1) = \sum (-1)^k k^2 A_k = \mathbf{v}_3^T \mathbf{A} = 0, \quad (\text{B3})$$

$$\sum A_k T'_k(1) = \sum k^2 A_k = \mathbf{v}_4^T \mathbf{A} = 0. \quad (\text{B4})$$

In the basis $\{T_0(2y - 1), \dots, T_{k+4}(2y - 1)\}$, T_{k+4} is the unit basis vector $\hat{\mathbf{e}}_{k+4}$. We subtract its orthogonal projection onto the four-dimensional subspace $\{\mathbf{v}_1, \dots, \mathbf{v}_4\}$ to obtain the coefficients of $Y_k(y)$ in the basis $\{T_0(2y - 1), \dots, T_{k+4}(2y - 1)\}$. This determines $Y_k(y)$.

-
- [1] R. B. Bird, W. E. Stewart, and E. N. Lightfoot, *Transport Phenomena* (John Wiley & Sons, Hoboken, NJ, 2007).
 [2] T. L. Bergman, T. L. Bergman, F. P. Incropera, D. P. Dewitt, and A. S. Lavine, *Fundamentals of Heat and Mass Transfer* (John Wiley & Sons, Hoboken, NJ, 2011).
 [3] J. H. Lienhard, *A Heat Transfer Textbook* (Courier Corporation, Chelmsford, MA, 2013).

-
- [4] T. Dauxois, T. Peacock, P. Bauer, C. P. Caulfield, C. Cenedese, C. Gorié, G. Haller, G. N. Ivey, P. F. Linden, E. Meiburg *et al.*, Confronting grand challenges in environmental fluid mechanics, *Phys. Rev. Fluids* **6**, 020501 (2021).
- [5] F. Marcotte, C. R. Doering, J.-L. Thiffeault, and W. R. Young, Optimal heat transfer and optimal exit times, *SIAM J. Appl. Math.* **78**, 591 (2018).
- [6] R. K. Shah and A. L. London, *Laminar Flow Forced Convection in Ducts: A Source Book for Compact Heat Exchanger Analytical Data* (Academic Press, London, 2014).
- [7] A. Glezer, R. Mittal, and S. Alben, Enhanced forced convection heat transfer using small scale vorticity concentrations effected by flow driven, aeroelastically vibrating reeds, technical report, Georgia Institute of Technology Atlanta United States, 2016.
- [8] Y. Kuwata, Dissimilar turbulent heat transfer enhancement by Kelvin-Helmholtz rollers over high-aspect-ratio longitudinal ribs, *J. Fluid Mech.* **952**, A21 (2022).
- [9] S. Pirozzoli and D. Modesti, Direct numerical simulation of one-sided forced thermal convection in plane channels, *J. Fluid Mech.* **957**, A31 (2023).
- [10] Q. Zhou, R. J. A. M. Stevens, K. Sugiyama, S. Grossmann, D. Lohse, and K.-Q. Xia, Prandtl–blausius temperature and velocity boundary-layer profiles in turbulent Rayleigh–Bénard convection, *J. Fluid Mech.* **664**, 297 (2010).
- [11] D. Sondak, L. M. Smith, and F. Waleffe, Optimal heat transport solutions for Rayleigh–Bénard convection, *J. Fluid Mech.* **784**, 565 (2015).
- [12] S. Toppaladoddi, S. Succi, and J. S. Wettlaufer, Roughness as a Route to the Ultimate Regime of Thermal Convection, *Phys. Rev. Lett.* **118**, 074503 (2017).
- [13] X. Zhu, V. Mathai, R. J. A. M. Stevens, R. Verzicco, and D. Lohse, Transition to the Ultimate Regime in Two-Dimensional Rayleigh–Bénard Convection, *Phys. Rev. Lett.* **120**, 144502 (2018).
- [14] B. Wen, D. Goluskin, M. LeDuc, G. P. Chini, and C. R. Doering, Steady Rayleigh–Bénard convection between stress-free boundaries, *J. Fluid Mech.* **905**, R4 (2020).
- [15] G. Wang, L. Santelli, R. Verzicco, D. Lohse, and R. J. A. M. Stevens, Off-centre gravity induces large-scale flow patterns in spherical Rayleigh–Bénard convection, *J. Fluid Mech.* **942**, A21 (2022).
- [16] T. Solano, J. C. Ordonez, and K. Shoele, Natural convection in vertical enclosures with conjugate boundary conditions, *J. Fluid Mech.* **946**, A17 (2022).
- [17] P. Hassanzadeh, G. P. Chini, and C. R. Doering, Wall to wall optimal transport, *J. Fluid Mech.* **751**, 627 (2014).
- [18] S. Alben, Improved convection cooling in steady channel flows, *Phys. Rev. Fluids* **2**, 104501 (2017).
- [19] S. Alben, Optimal convection cooling flows in general 2d geometries, *J. Fluid Mech.* **814**, 484 (2017).
- [20] A. N. Souza, I. Tobasco, and C. R. Doering, Wall-to-wall optimal transport in two dimensions, *J. Fluid Mech.* **889**, A34 (2020).
- [21] I. Tobasco and C. R. Doering, Optimal Wall-to-Wall Transport by Incompressible Flows, *Phys. Rev. Lett.* **118**, 264502 (2017).
- [22] C. R. Doering and I. Tobasco, On the optimal design of wall-to-wall heat transport, *Commun. Pure Appl. Math.* **72**, 2385 (2019).
- [23] A. N. Souza, An optimal control approach to bounding transport properties of thermal convection, Ph.D. thesis, University of Michigan, 2016.
- [24] S. Motoki, G. Kawahara, and M. Shimizu, Maximal heat transfer between two parallel plates, *J. Fluid Mech.* **851**, R4 (2018).
- [25] S. Motoki, G. Kawahara, and M. Shimizu, Optimal heat transfer enhancement in plane Couette flow, *J. Fluid Mech.* **835**, 1157 (2018).
- [26] A. Kumar, Three dimensional branching pipe flows for optimal scalar transport between walls, [arXiv:2205.03367](https://arxiv.org/abs/2205.03367).
- [27] H. Lamb, *Hydrodynamics* (Cambridge University Press, Cambridge, UK, 1932).
- [28] L. M. Milne-Thomson, *Theoretical Hydrodynamics*, 5th ed. (Macmillan, New York, 1968).
- [29] J. R. R. A. Martins and A. Ning, *Engineering Design Optimization* (Cambridge University Press, Cambridge, UK, 2021).
- [30] C. T. Kelley, *Iterative Methods for Optimization* (SIAM, Philadelphia, PA, 1999).